# Multiscale Modelling and Nonlinear Simulation of Vascular Tumour Growth: Supplementary Materials

**Paul Macklin · Stephen McDougall**★ **·
Alexander R. A. Anderson · Mark A.
J. Chaplain · Vittorio Cristini · John
Lowengrub**★

**Abstract** In this article, we present a new multiscale mathematical model for solid tumour growth which couples an improved model of tumour invasion with a model of tumour-induced angiogenesis. We perform nonlinear simulations of the multi-scale model that demonstrate the importance of the coupling between the development and remodelling of the vascular network, the blood flow through the network and the tumour progression. Consistent with clinical observations, the hydrostatic stress generated by tumour cell proliferation shuts down large portions of the vascular network dramatically affecting the flow, the subsequent network remodelling, the delivery of nutrients to the tumour and the subsequent tumour progression. In addition, extracellular matrix degradation by tumour cells is seen to have a dramatic affect on both the development of the vascular network and the growth response of the tumour. In

★ Corresponding Authors

Paul Macklin
School of Health Information Sciences, U. of Texas Health Science Center at Houston, USA
E-mail: Paul.T.Macklin@uth.tmc.edu          web: http://biomathematics.shis.uth.tmc.edu

Stephen McDougall
Department of Petroleum Engineering, Heriot-Watt University, Edinburgh, Scotland
E-mail: steve.mcdougall@pet.hw.ac.uk
web: http://www.pet.hw.ac.uk/aboutus/staff/pages/mcdougall_s.htm

Alexander R.A. Anderson
Division of Mathematics, University of Dundee, Scotland
E-mail: anderson@maths.dundee.ac.uk     web: http://www.maths.dundee.ac.uk/∼sanderso/

Mark A.J. Chaplain
Division of Mathematics, University of Dundee, Scotland
E-mail: chaplain@maths.dundee.ac.uk     web: http://www.maths.dundee.ac.uk/∼chaplain/

Vittorio Cristini
School of Health Information Sciences, U. of Texas Health Science Center at Houston, USA
M.D. Anderson Cancer Center, Houston, TX, USA
E-mail: Vittorio.Cristini@uth.tmc.edu          web: http://cristinilab.shis.uth.tmc.edu

John Lowengrub
Mathematics Department, University of California, Irvine, CA 92697-3875, USA
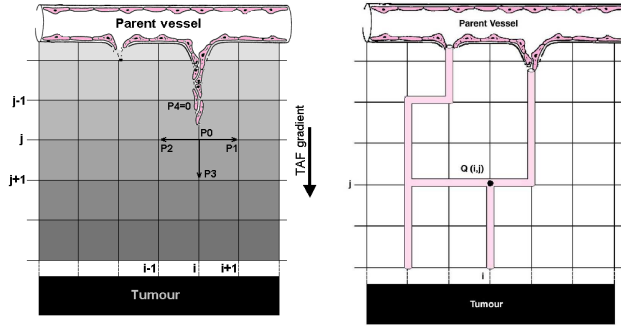E-mail: lowengrb@math.uci.edu          web: http://math.uci.edu/∼lowengrb

**Fig. 1 left:** A schematic diagram of the basic network model of tumour-induced angiogenesis. The P1, P2, P3, P4 denote the probabilities of the sprout EC moving in the coordinate directions. P0 denotes the probability of remaining stationary. Reprinted with permission from [18]. **right:** A schematic representation of the neo-vessels superimposed on the computational grid used for the flow calculation (after [18]).

particular, the newly developing vessels tend to encapsulate, rather than penetrate, the tumour and are thus less effective in delivering nutrients.

**Keywords** solid tumour · avascular growth · angiogenesis · vascular growth · multiscale mathematical model

# 1 Further Details on the Network Model

## 1.1 Further Schematics

Schematic figures of the basic vascular network model and the underlying computational grid for the flow calculation are given in Fig. 1.

## 1.2 Further Blood Viscosity Details

In Eq. 22 in Section 2.2.1, the apparent viscosity is given by

$$\mu_{\text{apparent}} = \mu_{\text{plasma}} \cdot \mu_{\text{rel}},$$

$$\mu_{\text{rel}}(R,h) = \tag{1}$$

$$\mu_{\text{rel}}(R,h) = \left(1 + (\mu_{0.45} - 1) f\left(h, \frac{R}{R^*}\right) \left(\frac{2\frac{R}{R^*}}{2\frac{R}{R^*} - 1.1}\right)^2\right) \left(\frac{2\frac{R}{R^*}}{2\frac{R}{R^*} - 1.1}\right)^2 \tag{2}$$

where $\mu_{\text{plasma}}$ is the plasma viscosity, $\mu_{\text{rel}}$ is the relative viscosity, $\mu_{0.45}$ is the (nondimensional) viscosity corresponding to the normal value of the discharge haematocrit (i.e., $h = \overline{H}_D = 0.45$), $R$ is the dimensional vessel radius (in $\mu$m), $R^*$ is a radius scale factor (taken to be equal to 1 $\mu$m), and $f(h, R)$ is a modulating function of the haematocrit and vessel radius. These effects are modelled by:

| [TAF] / TAF$_{\mathrm{max}}$ | WSS / $\tau_{\mathrm{max}}$ | | | | |
|---|---|---|---|---|---|
| | [0,0.2) | [0.2,0.4) | [0.4,0.6) | [0.6,0.8) | [0.8,1.0] |
| [0.0,0.3) | 0.00 | 0.00 | 0.00 | 0.00 | 0.00 |
| [0.3,0.5) | 0.00 | 0.02 | 0.04 | 0.06 | 0.08 |
| [0.5,0.7) | 0.00 | 0.03 | 0.06 | 0.09 | 0.12 |
| [0.7,0.8) | 0.00 | 0.04 | 0.08 | 0.12 | 0.16 |
| [0.8,1.0] | 0.00 | 0.10 | 0.20 | 0.30 | 0.40 |

**Table 1** Vessel branching probabilities according to the local TAF ($T$) concentration and to the magnitude of the local wall shear stress ($\tau_w$). TAF$_{\mathrm{max}}$ ($T_{\mathrm{max}}$) is the maximum TAF concentration and $\tau_{\mathrm{max}} = 5$ Pa (50 dynes/cm$^2$), the maximum shear stress derived from preliminary flow simulations.

$$\mu_{0.45} = 6e^{-0.17R/R^*} - 2.44e^{-0.06(2R/R^*)^{0.645}} + 3.2,$$

$$f\left(h, \frac{R}{R^*}\right) = \frac{(1-h)^{C(R/R^*)} - 1}{\left(1 - \overline{H}_D\right)^{C(R/R^*)} - 1},$$

$$C\left(\frac{R}{R^*}\right) = \left(e^{-1.5\times 10^{-7} R/R^*} + 0.8\right)\left(\frac{1}{1 + 10^{-23}(2R/R^*)^{12}} - 1\right)$$

$$+ \frac{1}{1 + 10^{-23}(2R/R^*)^{12}}. \tag{3}$$

The apparent blood viscosity (e.g. Eq. 22 in Section 2.2.2 in the main text) generally increases with decreasing capillary radius, although the precise relationship is nonlinear since it is actually haematocrit-dependent.

1.3 Further Wall Shear Stress Details

The combined effects of the local wall shear stress and TAF concentration upon vessel branching probability have been implemented in the model as described in Table 1 in the supplement. In the absence of quantitative experimental data, the probabilities chosen for the vessel branching process have been defined on a qualitative basis and reflect the combined influence of the wall shear stress (WSS) and local TAF concentration. High values of WSS in tandem with high local TAF concentrations lead to a higher branching probability, whilst lower values of one or both of WSS and TAF concentration lead to lower branching probability. For each range of WSS (linearly distributed in [0,1]), the corresponding TAF probability profile has been obtained via a linear scaling of the values reported in [19, 28, 29]. As mentioned above, in the absence of WSS, TAF-dependent sprout tip branching is the only means by which a migrating vessel can bifurcate. Sprout tip branching is performed using the algorithm developed by Anderson and Chaplain [2] and the corresponding tip branching probabilities are shown in Table 2.

## 2 Parameters and Nondimensionalizations used in the Simulations

In Table 3, we summarize the nondimensional variables used in the simulations. We give nondimensional parameters and their values in Tables 4-7.

| TAF Concentration | Sprout Tip Branching Probability |
|:---:|:---:|
| $[0, 0.3]$ | 0.0 |
| $(0.3, 0.5]$ | 0.2 |
| $(0.5, 0.7]$ | 0.3 |
| $(0.7, 0.8]$ | 0.4 |
| $(0.8, 1.0]$ | 1.0 |

**Table 2** Sprout tip branching probabilities as a function of the local TAF concentration

| Biological Quantity | Nondimensional Variable | Scaled By |
|:---:|:---:|:---|
| Oxygen concentration | $\sigma$ | $\sigma^*$, the oxygen level in well-oxygenated tissue (assumed to be the same as the oxygen level in the blood vessels) |
| Proliferation-induced biomechanical pressure | $P$ | $\lambda_M \ell^2 / \mu^*$, where $mu^*$ is a characteristic mobility value and $\lambda_M$ is the mitosis rate |
| Tumour-secreted angiogenic growth factor (TAF) | $T$ | $T^*$, the concentration of TAF secreted by tumour cells |
| Matrix degrading enzyme (MDE) | $M$ | $M^*$, the concentration of MDE secreted by tumour cells |
| Extracellular matrix (ECM) | $E$ | $E^*$, the concentration of ECM secreted by tumour cells |
| Original extracellular matrix | $E_0$ | $E^*$, the concentration of ECM secreted by tumour cells |
| Endothelial cell (EC) density | $n$ | $n^*$, a characteristic density of ECs |
| Pre-existing blood vessel density | $B_{\mathrm{pre}}$ | $B_{\mathrm{pre}}^*$, a characteristic density of of pre-existing vessels (e.g., value at the initial time) |

**Table 3** The variables in the tumour invasion model and their nondimensionalisation.

## 3 Details of the stimuli that affect the vessel radius in the adaptive dynamic tumour-induced angiogenesis model

***Wall shear stress*** – Many studies show that vessels adapt their radius in order to maintain a constant level of wall shear stress (e.g., [26, 23, 24, 4]). Hence vessel radius tends to increase with increasing wall shear stress, whilst wall shear stress decreases with increasing radius. The non-dimensional wall shear stress stimulus can be described by a logarithmic law as

$$S_{\mathrm{WSS}} = \log\left( \left( \tau_w + \tau_{\mathrm{ref}} \right) / \tau_w^* \right), \tag{4}$$

where $\tau_w = \frac{4\mu_{\mathrm{rel}}(R,h)}{\pi R^3} \left| \dot{Q} \right|$ is the actual wall shear stress in a vessel segment, $\dot{Q}$ is the flow rate in the vessel under consideration, $\tau_{\mathrm{ref}}$ is a constant included to avoid singular behaviour at low shear rates, and $\tau_w^*$ is a wall shear stress scale factor [23]. Dimensional stresses are in dynes/cm2.The dimensional wall shear stress calculated in the parent vessel of our computational model is of the order 4 Pa (40 dynes/cm$^2$) and capillary values are less than 2 Pa (20 dynes/cm$^2$), in agreement with those measured experimentally in the dog by Kamiya et al. [11]. Adaptation in response to the wall shear stress stimulus alone tends to reinforce a single path in the network composed of a few well-established fully dilated vessels–corresponding to the main flowing backbone

| Biological Quantity | Nondimensional Parameter | Scaled By | Value used in simulations |
|---|---|---|---|
| Uptake rate of oxygen in proliferating tumour region | $\bar{\lambda}_\sigma$ | $\lambda_\sigma^*$, the characteristic rate of oxygen uptake in the proliferating tumour region | 1 |
| Uptake rate of oxygen in host microenvironment | $\bar{\lambda}_{\text{tissue}}$ | $\lambda_\sigma^*$ | 0.25 |
| Uptake rate oxygen in quiescent (hypoxic) tumour region | $\bar{\lambda}_H$ | $\lambda_\sigma^*$ | 0.5 |
| Decay rate of oxygen in necrotic tumour region | $\bar{\lambda}_N$ | $\lambda_\sigma^*$ | 0.25 |
| Rate of blood-tissue oxygen transfer (extravasation) from pre-existing vessels | $\bar{\lambda}_{\text{pre}}^\sigma$ | $\lambda_\sigma^*$ | 0.25 |
| Rate of blood-tissue oxygen transfer (extravasation) from neo-vessels | $\bar{\lambda}_{\text{neo}}^\sigma$ | $\lambda_\sigma^*$ | 20 |
| Lower cutoff of original ECM, used in uptake in host microenvironment | $E_0^{\text{right cutoff}}$ | $E^*$, the concentration of ECM secreted by tumour cells | 1.0 |
| Upper cutoff of original ECM, used in uptake in host microenvironment | $E_0^{\text{left cutoff}}$ | $E^*$ | 0.625 |
| Characteristic value of discharge haematocrit | $\overline{H}_D$ | Already nondimensional | 0.45 |
| Minimum value of haematocrit needed for extravasation | $\bar{h}_{\text{min}}$ | Already nondimensional | 0.05 |
| Characteristic *dimensional* value of pressure in the neo-vessels (Eq. 6) | $\overline{P}_{\text{vessel}}$ | —— | 5000 Pa |
| Apoptosis rate | $A$ | $\lambda_m$, the mitosis rate | 0 |
| Scaling factor for hydrostatic (mechanical) pressure cutoff (Eq. 6) | $\overline{P}_{\text{scale}}$ | | 0.33 |
| Necrosis rate | $G_N$ | $\lambda_m$ | 0.3 |
| Tumour aggressiveness (adhesion) rate | $G$ | $\lambda_m$ | 40 |
| Minimum haptotaxis rate | $\bar{\chi}_{E,\text{min}}$ | $\chi_E^* E^*/(\ell^2 \lambda_m)$, where $\ell$ is the length scale | 0 |
| Maximum haptotaxis rate | $\bar{\chi}_{E,\text{max}}$ | $\chi_E^* E^*/(\ell^2 \lambda_m)$ | 0.25 |
| Maximum value of ECM used in haptotaxis coefficient (Eq. 15) | $\overline{E}_{\text{max cutoff}}^\chi$ | $E^*$ | 0.1 |
| Minimum value of ECM used in haptotaxis coefficient (Eq. 15) | $\overline{E}_{\text{min cutoff}}^\chi$ | $E^*$ | 0.9 |

**Table 4** Values of the parameters for the tumour invasion model–Eqs. 1-20. This table is continued in Table 5.

| Biological Quantity (continued) | Nondimensional Parameter (continued) | Scaled By (continued) | Value used in simulations (continued) |
|---|---|---|---|
| Minimum tumour mobility (response to hydrostatic/mechanical pressure) | $\overline{\mu}_{\text{min}}$ | $\mu^*$, a characteristic value of mobility | 1.0 |
| Maximum tumour mobility (response to hydrostatic/mechanical pressure) | $\overline{\mu}_{\text{max}}$ | $\mu^*$ | 4.0 |
| Minimum value of ECM used in mobility coefficient (Eq. 16) | $E^{\mu}_{\text{min cutoff}}$ | $E^*$ | 0 |
| Maximum value of ECM used in mobility coefficient (Eq. 16) | $E^{\mu}_{\text{max cutoff}}$ | $E^*$ | 1.0 |
| Oxygen diffusion coefficient | $\overline{\overline{D}}_{\sigma}$ | $D^*_{\sigma}$, a characteristic dimensional oxygen diffusion coefficient | 1.0 |
| MDE diffusion coefficient | $\overline{\overline{D}}_M$ | $\ell^2 \lambda_m$ | 1.0 |
| Production rate of MDE by tumour cells | $\overline{\lambda}^M_{\text{prod.}}$ | $\lambda_m$ | 100 |
| Natural decay of MDE | $\overline{\lambda}^M_{\text{decay}}$ | $\lambda_m$ | 10 |
| Production rate of MDE by EC sprout tips | $\overline{\lambda}^M_{\text{spr. prod.}}$ | $\lambda_m M^*$ | 1.0 |
| Rate of degradation of ECM by MDE | $\overline{\lambda}^E_{\text{degradation}}$ | $\lambda_m/M^*$ | 0.01 (Figs. 2-9) 1.0 (Figs. 10-16) |
| Rate of production of ECM by tumour cells | $\overline{\lambda}^E_{\text{prod.}}$ | $\lambda_m$ | 0.1 (Figs. 2-9) 2.72 (Figs. 10-16) |
| Rate of production of ECM by EC sprout tips | $\overline{\lambda}^E_{\text{spr. prod.}}$ | $\lambda_m/E^*$ | 0.1 |
| Rate of degradation of pre-existing blood vessels | $\overline{\lambda}^B_{\text{degradation}}$ | $\lambda_m/M^*$ | 0.02 (Figs. 2-9) 1.0 (Figs. 10-16) |
| TAF diffusion coefficient | $\overline{\overline{D}}_T$ | $D^*\sigma$ | 1.0 |
| Rate of TAF production by hypoxic tumour cells | $\overline{\lambda}^T_{\text{prod.}}$ | $\lambda^*\sigma$ | 100 |
| Rate of natural decay of TAF | $\overline{\lambda}^T_{\text{decay}}$ | $\lambda^*\sigma$ | 0.01 |
| Rate of binding of TAF by EC sprout tips | $\overline{\lambda}^T_{\text{binding}}$ | $\lambda^*_{\sigma}$ | 0.025 |

**Table 5** Values of the parameters for the tumour invasion model (continued)–Eqs. 1-20. This table is continued from Table 4.

| Biological quantity | Nondimensional Parameter | Scaled by | Value used in simulations |
|---|---|---|---|
| Random motion of EC | $D$ | $\ell^2 \lambda_m$ | $3.5 \times 10^{-4}$ |
| Chemotactic response of EC sprout tip | $\overline{\chi}^T_{\text{sprout}}$ | $\ell^2 \lambda_m / T^*$ | 0.38 |
| Decrease in chemotactic sensitivity | $\delta$ | $1/T^*$ | 0.6 |
| Haptotactic response of EC sprout tip | $\overline{\chi}^E_{\text{sprout}}$ | $\ell^2 \lambda_m / E^*$ | 0.16 |
| Response rate of neo-vessel radius to intravascular pressure | $k_p$ | $k_w$, the response rate of the neo-vessel radius to wall shear stress | 0.1 |
| Response rate of neo-vessel radius to metabolic stimulus | $k_m$ | $k_w$ | 0.07 |
| Natural shrinking tendency of neo-vessel radius | $\bar{k}_s$ | Already nondimensional | 0.35 |

**Table 6** Values of the non-dimensional parameters for the angiogenesis model–Eqs. 21-25.

| Biological Quantity | Dimensional Parameter | Value used in simulations |
|---|---|---|
| *Dimensional* neo-vascular radius scale factor Eq. 22 | $R^*$ | $1 \times 10^{-6}$ m |
| *Dimensional* wall shear stress scale factor | $\tau_w^*$ | 0.1 Pa |
| *Dimensional* wall shear stress regularization factor | $\tau_{\text{ref}}$ | 0.0103 Pa |
| *Dimensional* intravascular pressure stress scale factor | $\tau_e^*$ | 0.1 Pa |
| *Dimensional* natural shrinking tendency scale factor | $\tau_s^*$ | 1 Pa |
| *Dimensional* intravascular pressure scale factor | $P^*_{\text{vessel}}$ | 103 Pa |
| Flow rate in parent vessel | $\dot{Q}_{\text{ref}}$ | $1.909 \times 10^{-11}$ m$^3$/s |
| Threshold minimum neo-vessel radius for pressure cutoff (Eq. 25) | $R_{\text{min}}$ | $6 \times 10^{-6}$ m |

**Table 7** Values of the dimensional parameters for the angiogenesis model–Eqs. 21-25.

of the vasculature–whilst simultaneously eliminating the low-flow paths. However, the resulting network is "unstable" in the sense that there is no consistent balance for the radius and flow distribution achieved when $S_{\text{WSS}}$ is considered in isolation.

***Intravascular pressure*** – Intravascular pressure is another key stimulus for vascular adaptation. Pries et al. have experimentally observed on the rat mesentery the dependence of the magnitude of the wall shear stress with the local intravascular pressure ($P_{\text{vessel}}$) [25]. They proposed a parametric description of their experimental data, which exhibits a sigmoidal increase of the wall shear stress with increasing pressure through the following. The sensitivity of the corresponding (non-dimensionall) stimulus to intravascular pressure is then described by:

$$S_p = k_p \log \left( \tau_e \left( P_{\text{vessel}}/P^*_{\text{vessel}} \right) / \tau^*_e \right), \tag{5}$$

where $\tau_e \left( P_{\text{vessel}}/P^*_{\text{vessel}} \right) / \tau^*_e = 10^3 - 860 \exp \left( -5000 \left[ \log \left( \log P_{\text{vessel}}/P^*_{\text{vessel}} \right) \right]^{5.4} \right)$, $\tau^*_e$ is an intravascular pressure stress scale factor (note that $\tau^*_e$ itself is not needed for the simulation as the above formula is used), $P^*_{\text{vessel}}$ vessel P is a pressure scale factor, and $k_p$ is rate of response of the radius to the pressure stimulus.

***Metabolic haematocrit-related stimulus*** – The metabolic stimulus effectively stabilises the adapting network by stimulating vessel growth in areas of the vascular bed exhibiting low flow. The non-dimensional stimulus is once again described by a logarithmic law given by:

$$S_m = k_m \log \left( \frac{\dot{Q}_{\text{ref}}}{\dot{Q}h} + 1 \right), \tag{6}$$

where $k_m$ is a constant characterizing the relative intensity of the metabolic stimulus, and $\dot{Q}_{\text{ref}}$ is the flow rate in the parent vessel.

***Natrual shrinking tendency*** – The natural reaction of the basal lamina is thought to counter any increase in vessel diameter and can be modelled by [26]:

$$S_s = k_s \log \left( \tau_s / \tau^*_s \right), \tag{7}$$

where $\tau_s = \exp \left( -\overline{k}_s / k_s \right)$, $\overline{k}_s$ is a constant and $\tau^*_s$ is a shrinking tendency scale factor (taken to be $\tau^*_s = 1$ Pa). Note that since $\tau^*_s = 1$ Pa, $k_s$ no longer appears in Eq. 24 and instead we obtain $S_s = -\overline{k}_s$.

To summarise, the conditions for vessel branching in the DATIA model are as follows: (i) the likelihood of a vessel branching increases with both the local TAF concentration *and* the magnitude of the shear stress affecting the vessel wall; (ii) the vessel must reach a certain level of maturation before it is able to branch, although branching cannot occur once a basal lamina has formed around a vessel [5,3]. In the simulations presented here, however, there is no upper limit on the age of vessels that are allowed to branch. This models the case in which the continued tumour-induced angiogenic response prevents the formation of basal lamina. This effect will be considered in a future work.

## 4 Numerical techniques for tumour invasion model

***The ghost cell method*** – The reaction-diffusion equations describing nutrient transport, the pressure equilibration, the matrix degrading enzyme evolution and tumour angiogenic factor distribution may be written generically in the form:

$$\frac{\partial v}{\partial \tau} = \nabla \cdot (D(x,v)\nabla v) + f_R(x,v)v + f_S(x,v), \tag{8}$$

where $v = \sigma$, $P$, $M$ or $T$ and $\tau$ is either a pseudo-time variable (in the case of the elliptic/quasi-steady equations for nutrient, pressure and angiogenic factor) or is the

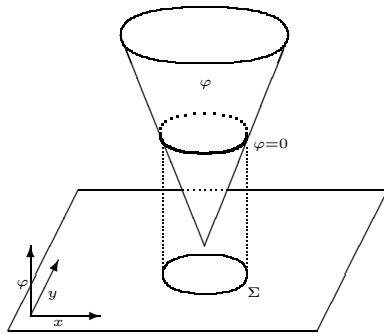**Fig. 2** Representing an ellipse as the zero contour of a level set function $\phi$.

real time (in the case of the MDE equation). Note that without loss of generality, $f_R$ is assumed to be non-positive.

We discretize Eq. 8 in (pseudo/real) time using the backward Euler method and lag the dependence of the diffusion coefficient $D$, reaction $f_R$ and source $f_S$ terms upon $v$. Away from interfaces, Eq. 8 is discretized in space using a centered finite difference scheme. For quantities that are smooth (i.e. $\sigma$, $M$, $E$ or $T$) centered differences are used throughout the domain. For the pressure, however, the jump conditions in Eqs. 11 and 12 need to be correctly incorporated and the difference stencils are modified near $\Sigma$ accordingly [13,14,16]. Note that we assume that there are no jumps across $\Sigma_N$ and thus no stencil modification is needed near $\Sigma_N$.

The stencil is modified in the following way. Whenever the boundary $\Sigma$ intersects the computational stencil, we replace points that are outside of the boundary with "ghost" points (denoted by hats) that are extrapolated from within the region where we also use the jump boundary condition, i.e.

$$P_\ell - P_r = -\frac{1}{G}\mathrm{sgn}(\phi)\kappa\left(\mathbf{x}_\Sigma\right) \tag{9}$$

where the $-\mathrm{sgn}(\phi)$ ensures the jump condition is applied in the proper direction and is discretized using the approach in [30]. See Fig. 3. In Eq. 9, the curvature $\kappa$ is accurately obtained from the level-set function f (i.e., $\kappa = \nabla \cdot (\nabla\phi/|\nabla\phi|)$) even for complex interface morphologies using a geometry aware discretization we recently developed [14,16]. Further, Eq. 9 introduces non-grid points $P_r$ and $P_\ell$ into the discretization. However, taking into account the jump condition on the normal derivative in Eq. 12, one obtains two equations for the two variables $P_\ell$ and $P_r$ allowing them to be eliminated from the discretization. The normal vector $\mathbf{n} = \nabla\phi/|\nabla\phi|$ is also discretized using a geometry-aware method [16].

The normal jump in Eq. 12 is discretized by taking decomposing the normal derivative into components in the grid $(u_\ell, u_r)$ and off-grid (diagonal, $v_\ell, v_r$) directions (see Fig. 4) that involve $p_\ell$ and $p_r$ and carefully matching extrapolations from inside and outside of the tumour domain $\Omega$. This approach does not smear tangential derivatives- a problem that plagued earlier implementations of ghost cell methods. Indeed, this algorithm has tested better than 1.5-order accurate [16]; in contrast, previous ghost fluid and ghost cell methods (e.g., [12]) smear jumps in the tangential derivative and either fail to converge or are at best very low (sub-0.3) order accurate.
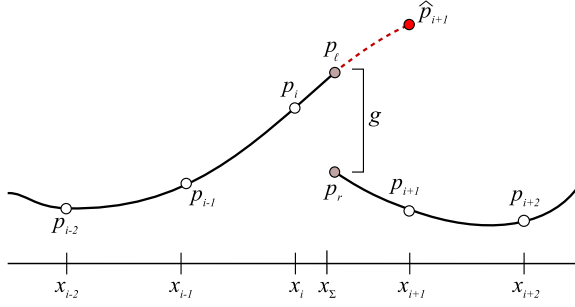
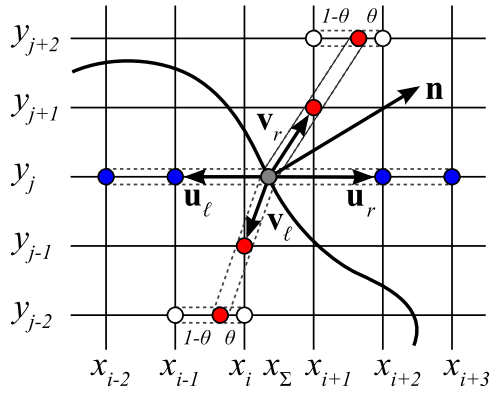**Fig. 3** Ghost cell extrapolation from one region into another.



**Fig. 4** Stencil for discretizing normal derivative jump conditions across a boundary.

The fully discrete version of Eq. 8 is solved using a nonlinear adaptive Gauss-Seidel-type iterative method (NAGSI). Because of the lagged form of the time discretization, there is no need to solve a large linear system at each iteration step. Instead, there is only a local solve which can be performed analytically. In the case of the time-dependent MDE equation, this is sufficient to advance to the next time step. For the nutrient, pressure and tumour angiogenic factor, however, Eq. 8 must be solved to steady state (within an error tolerance) and thus further iterations are necessary. To advance to steady state efficiently, we take advantage of the fact that as the solution converges, the numerical solution tends to change most on a small fraction of the computational nodes. Therefore, we can select computational nodes where the numerical solution is changing most rapidly and update only those nodes. This algorithm is very efficient and adaptivity typically yields about a 50% reduction in computational time [16].

***The level set method*** – Level set methods were first developed by Osher and Sethian [21] and have been used to study the evolution of moving, complex surfaces (see the books [27, 20] and the references therein). Level set methods have been previously used in the context of tumour growth by Macklin & Lowengrub [13–16], Zheng et al. [32], and Hogea et al. [8].

In the level set approach, instead of explicitly tracking the position of interfaces $\Sigma$ and $\Sigma_N$ and manually handling topology changes, the level set function is updated by solving a Hamilton-Jacobi partial differential equation, which automatically accounts for the interface motion and possible morphological changes of the interface.

The idea is as follows. Let $V$ be the outward normal velocity of the interface $\Sigma$ (e.g. see Eq. 13) and let $V_{\text{extension}}$ be an extension of $V$ off of the tumour boundary $\Sigma$ such that $V_{\text{extension}} = V$ on $\Sigma$. One possibility is to use $\mathbf{u}$, from Eq. 7, as the extension of $V$ off the interface. This is actually not done, as explained below. To update the position of the boundary $\Sigma$, we solve the Hamilton-Jacobi equation

$$\frac{\partial \phi}{\partial t} + V_{\text{extension}} |\nabla \phi| = 0. \tag{10}$$

Note that the position of the necrotic/viable interface $\Sigma_N$ is similarly obtained by evolving $\phi_N$ with an extension $V_{N,\text{extension}}$ of the necrotic velocity $V_N$ off the boundary $\Sigma_N$. We obtain the extension velocities using a bilinear extrapolation technique first presented in [13] that is constant in the normal direction to the interface. This can be thought of as a higher order version of the fast marching method (e.g. [1, 31]). An advantage of taking $V_{\text{extension}}$ to be constant in the normal direction is that distance functions are then preserved by Eq. 10. If instead $V_{\text{extension}} = \mathbf{u}$, this would not be the case. Even though theoretically $\partial V_{\text{extension}}/\partial n = 0$, it is still helpful to prevent accumulation of numerical error by reinitializing $\phi$ periodically to be a distance function by solving

$$\frac{\partial \phi}{\partial \tau} = \text{sgn}\left(\phi^0\right)\left(1 - |\nabla \phi|\right) \tag{11}$$

to steady state, where $\tau$ is pseudo-time and $\phi^0$ is the original level-set function prior to reinitialization. Finally, Eqs. 10 and 11 are discretized in time using first order Euler method and a third-order total variation-diminishing Runge-Kutta method (TVD-RK) [6,7], respectively. The former is used to reduce computational cost. In space, the $|\nabla \phi|$ is discretized using the fifth-order weighted essentially non-oscillatory (WENO) method [10,9].

Lastly, we update Eqs. 10 and 11 only near the interface using the narrow band/local level set technique [17,22] with a band size of $20\Delta x$.

For further details on the ghost cell/level-set algorithm, the reader is referred to [13,14,16].

## 5 Additional details of the invasion model: The interpolating functions

Several interpolation functions are used in the tumour invasion model. These are given below. In the oxygen uptake equation (2), the interpolation function $p_\sigma(E_0)$ is defined by

$$p_\sigma(E_0) = \begin{cases} 0 & E_0 < E_0^{\text{left cutoff}} \\ p(E_0) & E_0^{\text{left cutoff}} \leq E_0 \leq E_0^{\text{right cutoff}} \\ 0 & E_0 > E_0^{\text{right cutoff}} \end{cases},$$

and $p(E_0)$ is a cubic polynomial satisfying:

$$p\left(E_0^{\text{left cutoff}}\right) = 0 \ , \ p'\left(E_0^{\text{left cutoff}}\right) = 0$$
$$p\left(E_0^{\text{right cutoff}}\right) = 1 \ , \ p'\left(E_0^{\text{right cutoff}}\right) = 0.$$

In Eq. 2, $q_\sigma(\sigma)$ is a quartic polynomial chosen to satisfy

$$q_\sigma(\sigma_H) = \overline{\lambda}_V \ , \ q'_\sigma(\sigma_H) = 0,$$
$$q_\sigma\left(\tfrac{\sigma_H + \sigma_N}{2}\right) = \overline{\lambda}_H \ ,$$
$$q_\sigma(\sigma_N) = \overline{\lambda}_N \ , \ q'_\sigma(\sigma_N) = 0.$$

In Eq. 5, $p_{\text{cutoff}}$ is a cubic polynomial chosen to satisfy:

$$p_{\text{cutoff}}(0) = 0 \ , \ p'_{\text{cutoff}}(0) = 0,$$
$$p_{\text{cutoff}}(1) = 1 \ , \ p'_{\text{cutoff}}(1) = 0.$$

Both the haptotactic sensitivity and the mobility of the tumour cells involve interpolating functions. In Eq. 15, $p_\chi(E)$ is a quartic polynomial chosen to satisfy:

$$p_\chi\left(\overline{E}^{\chi}_{\text{min cutoff}}\right) = \overline{\chi}^E_{\text{min}} \ , \ p'_\chi\left(\overline{E}^{\chi}_{\text{min cutoff}}\right)$$
$$p_\chi\left(\frac{\overline{E}^{\chi}_{\text{min cutoff}} + \overline{E}^{\chi}_{\text{max cutoff}}}{2}\right) = \overline{\chi}^E_{\text{max}} \ ,$$
$$p_\chi\left(\overline{E}^{\chi}_{\text{max cutoff}}\right) = \overline{\chi}^E_{\text{min}} \ , \ p'_\chi\left(\overline{E}^{\chi}_{\text{max cutoff}}\right) = 0.$$

Finally, in Eq. 16, the function $p_\mu(E)$ is the cubic polynomial:

$$p_\mu\left(\overline{E}^{\mu}_{\text{min cutoff}}\right) = \overline{\mu}_{\text{max}} \ , \ p'_\mu\left(\overline{E}^{\mu}_{\text{min cutoff}}\right) = 0$$
$$p_\mu\left(\overline{E}^{\mu}_{\text{max cutoff}}\right) = \overline{\mu}_{\text{min}} \ , \ p'_\mu\left(\overline{E}^{\mu}_{\text{max cutoff}}\right) = 0.$$

## References

1. Adalsteinsson, D., Sethian, J.A.: The Fast Construction of Extension Velocities in Level Set Methods. J. Comput. Phys. **148**(1), 2–22 (1999). DOI 10.1006/jcph.1998.6090
2. Anderson, A.R.A., Chaplain, M.A.J.: Continuous and discrete mathematical models of tumor-induced angiogenesis. Bull. Math. Biol. **60**(5), 857–900 (1998). DOI 10.1006/bulm.1998.0042
3. Benjamin, L.E., Hemo, I., Keshet, E.: A plasticity window for blood vessel remodelling is defined by pericyte coverage of the preformed endothelial network and is regulated by pdgf-$\beta$ and vegf. Development (Camb.) **125**, 1591–8 (1998)
4. Fung, Y.C.: Biomechanics. Springer, New York (1993)
5. Gee, M.S., Procopio, W.N., Makonnen, S., Feldman, M.D., Yeilding, N.M., Lee, M.F.: Tumor vessel development and maturation impose limits on the effectiveness of anti-vascular therapy. Am. J. Pathol. **16**, 183–93 (2003)
6. Gottlieb, S., Shu, C.W.: Total Variation Diminishing Runge-Kutta Schemes. Math. Comp. **67**(221), 73–85 (1997). DOI 10.1090/S0025-5718-98-00913-2
7. Gottlieb, S., Shu, C.W., Tadmor, E.: Strong Stability-Preserving High-Order Time Discretization Methods. SIAM Review **43**(1), 89–112 (2001). DOI 10.1137/S003614450036757X
8. Hogea, C.S., Murray, B.T., Sethian, J.A.: Simulating complex tumor dynamics from avascular to vascular growth using a general level-set method. J. Math. Biol. **53**(1), 86–134 (2006). DOI 10.1007/s00285-006-0378-2
9. Jiang, G.S., Peng, D.: Weighted ENO Schemes for Hamilton-Jacobi Equations. SIAM J. Sci. Comput. **21**(6), 2126–2143 (2000). DOI 10.1137/S106482759732455X

10. Jiang, G.S., Shu, C.W.: Efficient Implementation of Weighted ENO Schemes. J. Comput. Phys. **126**(2), 202–228 (1996). DOI 10.1006/jcph.1996.0130
11. Kamiya, A., Bukhari, R., Togawa, T.: Adaptive regulation of wall shear stress optimizing vasular tree function. Bull. Math. Biol. **46**, 127–37 (1984)
12. Liu, X.D., Fedkiw, R., Kang, M.: A Boundary Condition Capturing Method for Poisson's Equation on Irregular Domains. J. Comput. Phys. **160**(1), 151–178 (2000). DOI 10.1006/jcph.2000.6444
13. Macklin, P., Lowengrub, J.S.: Evolving interfaces via gradients of geometry-dependent interior Poisson problems: application to tumor growth. J. Comput. Phys. **203**(1), 191–220 (2005). DOI 10.1016/j.jcp.2004.08.010
14. Macklin, P., Lowengrub, J.S.: An improved geometry-aware curvature discretization for level set methods: application to tumor growth. J. Comput. Phys. **215**(2), 392–401 (2006). DOI 10.1016/j.jcp.2005.11.016
15. Macklin, P., Lowengrub, J.S.: Nonlinear simulation of the effect of microenvironment on tumor growth. J. Theor. Biol. **245**(4), 677–704 (2007). DOI 10.1016/j.jtbi.2006.12.004
16. Macklin, P., Lowengrub, J.S.: A new ghost cell/level set method for moving boundary problems: Application to tumor growth. J. Sci. Comput. (2008). DOI 10.1007/s10915-008-9190-z. (in press)
17. Malladi, R., Sethian, J.A., Vemuri, B.C.: A fast level set based algorithm for topology-independent shape modeling. J. Math. Imaging Vision **6**(2-3), 269–289 (1996). DOI 10.1007/BF00119843
18. McDougall, S.R., Anderson, A.R.A., Chaplain, M.A.J.: Mathematical modelling of dynamic adaptive tumour-induced angiogenesis: Clinical implications and therapeutic targeting strategies. J. Theor. Biol. **241**(3), 564–589 (2006). DOI 10.1016/j.jtbi.2005.12.022
19. McDougall, S.R., Anderson, A.R.A., Chaplain, M.A.J., Sherratt, J.A.: Mathematical modelling of flow through vascular networks: implications for tumour-induced angiogenesis and chemotherapy strategies. Bull. Math. Biol. **64**(4), 673–702 (2002)
20. Osher, S., Fedkiw, R.: Level Set Methods and Dynamic Implicit Surfaces. Springer, New York, NY (2002)
21. Osher, S., Sethian, J.A.: Fronts propagating with curvature-dependent speed: algorithms based on Hamilton-Jacobi formulations. J. Comput. Phys. **79**(1), 12–49 (1988). DOI 10.1016/0021-9991(88)90002-2
22. Peng, D., Merriman, B., Osher, S., Zhao, H., Kang, M.: A PDE-Based fast local level set method. J. Comput. Phys. **155**(2), 410–438 (1999). DOI 10.1006/jcph.1999.6345
23. Pries, A.R., Reglin, B., Secomb, T.W.: Structural adaptation of microvascular networks: functional roles of adaptive responses. Am. J. Physiol. Heart Circ. Physiol. **281**, H101525 (2001)
24. Pries, A.R., Reglin, B., Secomb, T.W.: Structural adaptation of vascular networks: role of the pressure response. Hypertension **38**, 14769 (2001)
25. Pries, A.R., Secomb, T.W., Gaehtgens, P.: Design principles of vascular beds. Circulation Res. **77**, 1017–1023 (1995)
26. Pries, A.R., Secomb, T.W., Gaehtgens, P.: Structural adaptation and stability of microvascular netwoks: theory and simulation. Am. J. Physiol. Heart Circ. Physiol. **275**(44), H34960 (1998)
27. Sethian, J.A.: Level Set Methods and Fast Marching Methods. Cambridge University Press, New York, NY (1999)
28. Stéphanou, A., McDougall, S.R., Anderson, A.R.A., Chaplain, M.A.J.: Mathematical modelling of flow in 2D and 3D vascular networks: applications to anti-angiogenic and chemotherapeutic drug strategies. Math. Comp. Model. **41**(10), 1137–56 (2005). DOI 10.1016/j.mcm.2005.05.008
29. Stéphanou, A., McDougall, S.R., Anderson, A.R.A., Chaplain, M.A.J.: Mathematical modelling of the influence of blood rheological properties upon adaptive tumour-induced angiogenesis. Math. Comp. Model. **44**(1-2), 96–123 (2006). DOI 10.1016/j.mcm.2004.07.021
30. Sussman, M., Fatemi, E.: An Efficient, Interface Preserving Level Set Re-Distancing Algorithm and its Application to Interfacial Incompressible Fluid Flow. SIAM J. Sci. Comput. **20**(4), 1165–1191 (1999). DOI 10.1137/S1064827596298245
31. Zhao, H.K.: A fast sweeping method for eikonal equations. Math. Comp. **74**, 603–27 (2005)
32. Zheng, X., Wise, S.M., Cristini, V.: Nonlinear simulation of tumor necrosis, neovascularization and tissue invasion via an adaptive finite-element/level set method. Bull. Math. Biol. **67**(2), 211–259 (2005). DOI 10.1016/j.bulm.2004.08.001